**Geomechanics and Engineering**, *Vol. 38, No. 3 (2024) 261-273*
https://doi.org/10.12989/gae.2024.38.3.261

# The exact bearing capacity of strip footings on reinforced slopes using slip line method

Majd Tarraf[a] and Ehsan Seyedi Hosseininia*

*Department of Civil Engineering, Faculty of Engineering, Ferdowsi University of Mashhad, Mashhad, Iran*

(*Received February 3, 2023, Revised July 11, 2024, Accepted July 17, 2024*)

**Abstract.** This study presents a groundbreaking analytical approach to find an exact solution for the bearing capacity of strip footings on reinforced slopes, utilizing the two-phase approach and slip line method. The two-phase approach is considered as a generalized homogenization technique. The slip line method is leveraged to derive the stress field as a lower bound solution and the velocity field as an upper bound solution, thereby facilitating the attainment of an exact solution. The key finding points out the variation of the bearing capacity factor $N_\gamma$ with influencing factors including the backfill soil friction angle, the footing setback distance from the slope crest edge, slope angle, strength, and volumetric fraction of inclusion layers. The results are evaluated by comparing them with those of relevant studies in the literature considering analytical and experimental studies. Through the application of the two-phase approach, it becomes feasible to determine the tensile loads mobilized along the inclusion layers associated with the failure zone. It is attempted to demonstrate the results by utilizing non-dimensional graphs to clearly illustrate variable impacts on reinforced soil stability. This research contributes significantly to advancing geotechnical engineering practices, specifically in the realm of static design considerations for reinforced soil structures.

**Keywords:** bearing capacity; exact solution; footings/foundations; reinforced soils; setback distance; slip line method; two phase approach

## 1. Introduction

Due to limited available land, structures are often constructed near the edge of slopes, including applications like bridge abutments, buildings, and highways. Constructing strip footings near slope crests can lead to instability and reduced load-bearing capacity. Numerous studies have explored the performance of strip footings near slopes under static loading (Chakraborty and Kumar 2013, Luo and Bathurst 2017, Chakraborty *et al.* 2019, Afsharpour *et al.* 2022, Sarvesh *et al.* 2023).

The reinforced soil technique has proven beneficial, enhancing load-bearing capacity, economic efficiency, and construction ease. Experimental and numerical studies have assessed reinforced slopes under strip loading, highlighting the importance of analytical studies on the bearing capacity of footings on reinforced soil structures (Zhao 1996, Jahanandish and Keshavarz 2005, Ausilio 2014, Javdanian 2017, Acharyya and Dey 2018, Luo and Bathurst 2018, Halder and Chakraborty 2020, Wang *et al*. 2020, Ardakani and Namaei 2021, Ahmadi *et al*. 2022, Sarfarazi *et al.* 2022, Xu *et al.* 2022). The numerical analyses encompassed various methodologies, including limit equilibrium, limit analysis, method of stress characteristics, and finite element approaches. The limit equilibrium approach was utilized by Xie *et al.* (2019) to assess the ultimate bearing capacity of strip footings on a geosynthetic-reinforced soil slope. In a similar vein, Ausilio (2014) employed the kinematic theorem of the limit analysis, established within the pseudo-static method, to evaluate the seismic bearing capacity of shallow strip foundations situated in proximity to the crest of reinforced soil structures. The primary objective was to investigate the impact of different design parameters on the bearing capacity of these footings. Manna *et al.* (2021) introduced the kinematic approach of upper-bound limit analysis to assess the ultimate bearing capacity of rigid pavements constructed on reinforced soil embankments.

The Slip Line Method (SLM) offers a simplified approach to complex plastic problems without assuming failure surface geometry, making it ideal for analyzing rigid-plastic materials (Yu 2007). The method of stress characteristics is a specific case of SLM focusing solely on the stress field (Gholami and Seyedi Hosseininia 2017, Tarraf and Seyedi hosseininia 2023). Michalowski and Zhao (1995) employed the stress characteristics method to explore the ultimate stress field in reinforced soil structures under static state. To complement this research, Jahanandish and Keshavarz (2005) utilized the stress characteristics method to assess the seismic bearing capacity of a foundation placed on a slope reinforced with geosynthetics. However, their analysis was limited to the stress field, and considerations for the distance between the foundation and the slope crest edge were not addressed. Also, the reinforced soil mass was treated as a composite material in these works. The aim of these studies was to analyze stress characteristic fields to gain insights into areas of plasticity within the reinforced mass.

---

*Corresponding author, Professor
E-mail: eseyedi@um.ac.ir
[a]Ph.D. Student
E-mail: majd.tarraf@mail.um.ac.ir

http://www.techno-press.org/?journal=gae&subpage=7

ISSN: 2005-307X (Print), 2092-6219 (Online)

Apart from examining each element of reinforced soil individually in detail, the reinforced soil medium can also be viewed as a composite material with uniform yet directionally varying properties when observed on a larger scale. This behavior is a result of the arrangement of multiple soil layers and reinforcing elements in periodic patterns. Taking the analysis to a higher level, an innovative method known as the Multiphase Model has been introduced by de Buhan and Sudret (1999). This model extends the traditional homogenization technique by representing the composite as a combination of interacting mediums or "phases" at the macroscopic scale. In this conceptualization, reinforced soil is seen as a two-phase medium, where each point embodies both the soil matrix phase and the reinforcement phase. Each phase is associated with different kinematic properties, governed by an interaction law that dictates their interplay (Seyedi Hosseininia and Farzaneh 2010, Seyedi Hosseininia and Farzaneh 2010). In contrast to conventional homogenization techniques, the multiphase model effectively addresses both scale and boundary effects, providing a thorough understanding of the system (Hassine *et al.* 2008, Seyedi Hosseininia and Farzaneh 2011). The two-phase concept has proven successful in examining the behavior of reinforced soil structures, including piled raft (Nasrollahi and Seyedi Hosseininia 2019) and geosynthetic-reinforced soil walls under static and seismic loads (Honari and Seyedi Hosseininia 2016, Seyedi Hosseininia and Ashjaee 2018).

This study delves into the derivation of an exact solution of the bearing capacity of shallow strip footings adjacent to reinforced soil slopes in a static state, employing the two-phase approach and the Slip Line Method (SLM). By utilizing SLM, the critical slip surface is determined through the resolution of boundary value problems. Furthermore, by employing the theory of two-phase approach, it is possible to find the tensile loads mobilized along the inclusion layers corresponding to failure zone. A thorough parametric study is conducted to investigate the influence of various factors on bearing capacity. The study specifically scrutinizes parameters such as the setback distance of the footing from the slope crest edge, slope angle, and backfill soil friction angle. The analytical results are presented in non-dimensional graphs, offering valuable insights for preliminary design considerations.

## 2. Structural analysis methodology

The current investigation aims to ascertain the exact bearing capacity of a footing positioned on a reinforced slope and delineates a critical slip surface. To accomplish this objective, we utilize the two-phase approach along with the slip line method. In Fig. 1, a rigid footing, denoted by width B and located at a distance $S_b$ from the edge of a soil slope reinforced with inclusion layers, is depicted. The reinforced slope has a height H and inclined at an angle β to the horizontal plane. The geometric coordinates system (x-z) is centered on the slope surface, with x representing the horizontal axis and z the downward axis, as illustrated in Fig. 1. The soil mass with the weight (W) can slide down over the potential slip surface. The inclusion layers are evenly positioned horizontally inside the soil at intervals denoted by d.

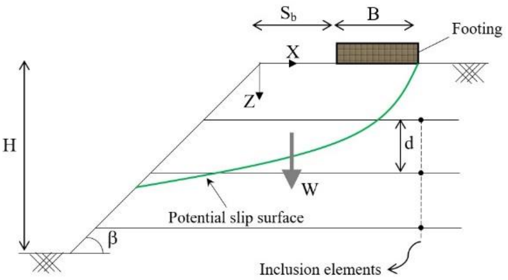

Fig. 1 Illustrative representation of a footing positioned on a reinforced soil slope

### 2.1 Key Foundations of the two-phase approach

In this investigation, the amalgamation of soil and inclusion layers is considered as a composite material utilizing the two-phase approach. Fig. 2 illustrates the concept of a two-phase material in the context of a reinforced soil slope. The reinforced soil is represented as a periodic medium with systematically positioned inclusion layers within the soil, as depicted in Fig. 2(a). The two-phase system provides a macroscopic representation of the composite material, presenting it as a blend of two continuous phases, as shown in Fig. 2(b). Each point in the material's geometry comprises a matrix phase representing the soil and a reinforcement phase indicating the presence of axial inclusion layers. In a two-phase material, each phase exhibits distinct characteristics, akin to those defined for individual constituents in a discrete form. Employing the theory of the virtual work method, the equilibrium equation is independently established for each phase, as elaborated below (de Buhan and Sudret 1999):

For the matrix phase

$$div\boldsymbol{\sigma}^m + \rho^m \mathbf{F}^m + \mathbf{I} = \mathbf{F}_I^m \tag{1a}$$

and for reinforcement phase:

$$div\boldsymbol{\sigma}^r + \rho^r \mathbf{F}^r - \mathbf{I} = \mathbf{F}_I^r \tag{1b}$$

In the provided equations, the superscripts "m" and "r" signify the matrix and reinforcement phases, respectively. The symbol $\mathbf{F}_I^i$ denotes inertial force (i = m, r). Boldface letters are used for tensor and vector representations. The stress tensor for each phase is denoted by $\boldsymbol{\sigma}$. The term $\rho^i\mathbf{F}^i$ represents the external (body) force vector applied to the phases, while $\mathbf{I}$ indicates the interaction force vector between the two phases. These equilibrium equations are complemented by stress boundary conditions specified on the individual boundary surfaces of each phase.

Summing Eqs. (1(a)) and (1(b)) yields the global equilibrium equation for a two-phase material, presented in the following form

$$div\boldsymbol{\Sigma} + \rho\mathbf{F} = \mathbf{F}_I \tag{2}$$

where $\boldsymbol{\Sigma} = \boldsymbol{\sigma}^m + \boldsymbol{\sigma}^r$ , $\rho\mathbf{F} = \rho\mathbf{F}^m + \rho\mathbf{F}^r$ , $\mathbf{F}_I = \mathbf{F}_i^m + \mathbf{F}_i^r$ . $\boldsymbol{\Sigma}$ represents the global stress tensor of a two-phase material, obtained by summing the partial stresses of both phases. Similarly, $\rho\mathbf{F}$ represents the global body force of the two-

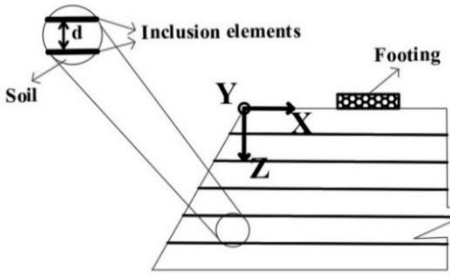

(a) In discrete form

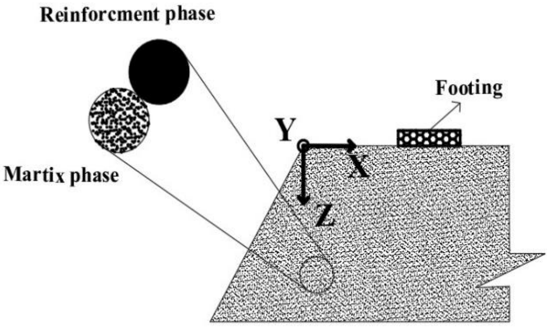

(b) Based on the two-phase approach

Fig. 2 Schematic illustration of a footing placed on a reinforced slope

phase material, and **F**$_I$ indicates the global inertial force of the two-phase material. The yield criterion of the two-phase material occurs due to the yielding of both the matrix phase (soil) and the reinforcement phase (inclusion layers).

### *2.1.1 Reinforcement phase*

The inclusion layers are treated as planar, indicating that their mechanical behavior is influenced solely by stress components within the inclusion plane (x-y plane in Fig. 2). Contributions from out-of-plane (inclusion plane x-y) component (z-direction) is not considered in this analysis (de Buhan and Sudret 1999). It is assumed that the planar inclusion exhibits only tensile behavior. The inclusion element's role as the reinforcement phase in the two-phase medium is defined by the concept of microscopic scale, as illustrated in Fig. 2. The volumetric reinforcement fraction, $\chi$, equals the volumetric ratio of the inclusion layers to the soil mass, given by $\chi=t/d$, where t is the inclusion thickness

The stress components $\sigma^r_i$ (i = x, y) in the reinforcement phase is obtained by multiplying the volumetric reinforcement fraction $\chi$ with the stress components $\sigma^{inc}_i$ (i = x, y) of the inclusion element. By considering the definition of the yield stress $\sigma^r_f$ in the reinforcement phase (as a macroscopic view) and the yield stress $\sigma^{inc}_f$ of the singular inclusion layer (as a microscopic view), the macro-microscopic stress relationship can be expressed as follows (Seyedi Hosseininia and Farzaneh 2010)

$$\sigma_i^r = \chi\sigma_i^{inc} \quad (i=x,y) \tag{3a}$$

$$\sigma_f^r = \chi\sigma_f^{inc} \tag{3b}$$

Taking into account the planar nature of the stress-strain relationship for the inclusion layer and neglecting the out-of-plane component, it becomes feasible to represent the behavior of this inclusion layer in a one-dimensional form with respect $\sigma^r_x$. The yield criterion function of the reinforcement phase ($f^r$) is formulated according to Seyedi Hosseininia and Farzaneh (2010)

$$f^r\left(\sigma_x^r\right)=\sigma_x^r-\sigma_f^r=0 \tag{4}$$

This study utilizes a parameter known as the mobilization coefficient , $\xi$, to compute the mobilised stress within the reinforcement phase, akin to the definition provided by Michalowski and Zhao (1995)

$$\xi=\frac{\sigma_x^r}{\sigma_f^r} \tag{5}$$

As the reinforcement phase does not endure compression, the range of variability for $\xi$ is confined to $-1 \le \xi \le 0$, considering compression as positive.

### *2.1.2 Matrix phase*

The soil volume within the reinforced soil medium far exceeds that of the inclusions. Hence, it is posited that the stress tensor of the matrix phase mirrors that of the soil itself. Employing the well-established Mohr-Coulomb failure criterion, the function ($f^m$) delineating the failure surface is defined in relation to parameters like the internal friction angle ($\phi$) and cohesion (c), as expressed below

$$f^m\left(\boldsymbol{\sigma}^m\right)=\sqrt{\frac{\left(\sigma_z^m-\sigma_x^m\right)^2}{4}+\left(\sigma_{xz}^m\right)^2}-\left(\frac{\sigma_x^m+\sigma_z^m}{2}\right)\sin\phi-c\cos\phi=0 \tag{6}$$

where ($\sigma^m_x$, $\sigma^m_z$ and $\sigma^m_{xz}$) are the matrix phase stress components. It is supposed that the out-of-plane stress component of the matrix phase (i.e., soil) is the intermediate one. The schematic representation of the stress Mohr circle and Coulomb failure surface is depicted in Fig. 3, where $p$ signifies the average stress, $R$ denotes the radius of the Mohr circle, and $\psi$ is the angle formed between the horizontal direction and the major principal stress direction $\sigma^m_1$.

### *2.1.3 Two-phase formulation*

By substituting Eq. (4) into Eq. (2), the elements of the global stress tensor ($\boldsymbol{\Sigma}$) of the reinforced soil medium are expressed as

$$\begin{cases}\Sigma_x=\sigma_x^m+\sigma_x^r\\ \Sigma_z=\sigma_z^m\\ \Sigma_{xz}=\sigma_{xz}^m\end{cases} \tag{7}$$

In a two-phase material, each phase can have distinct sets of kinematic properties. When the displacement and velocity fields of both phases are identical, the two-phase material can be treated simply as a homogenized material. In this study, on the one hand, we assume that the soil and the inclusion layers (matrix and reinforcement phases) have the same displacement fields. On the other hand,

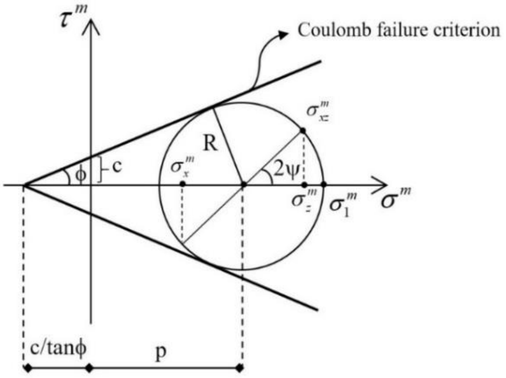

Fig. 3 The stress Mohr circle and Coulomb failure surface

Michalowski and Zhao (1995) applied the homogenization concept to derive the failure criterion for homogenized material for a planar medium.

They considered that the failure criterion is a function of ψ and the inclination of the inclusion layer with respect to the horizontal direction. Similarly, we employ the same concept in this study to elucidate the interaction between the matrix and reinforcement phases, with the inclusion layers oriented horizontally. Similarly, this study employs the same concept, wherein the inclusion layers are horizontal, and there is no slippage or relative displacement between the phases. It is worth noting that the assumption of an identical displacement field for the soil and inclusion layers corresponds only to the cases where the soil is dense and well compacted, a condition consistent with the real-world practice of reinforced soil slope construction. This assumption is supported by previous experimental and numerical studies in the literature (Afzali-Nejad *et al.* 2021). According to Fig. 3, the radius of the Mohr stress in the matrix phase (R) is impacted by the stress state in the reinforcement phase, contingent on the reinforcement inclination angle. Consequently, a functional form of R(ψ,p) can be postulated. Following the classification by Michalowski and Zhao (1995), three cases for the R value have been delineated.

In the first case, if $2\psi \le \frac{\pi}{2} - \phi$, indicating no influence of reinforcement (mobilization coefficient of the reinforcement strength is zero), failure is solely associated with the matrix phase $\xi = 0$. In this scenario, R is a function solely dependent on p.

$$R(p) = p\sin\phi + c\cos\phi \tag{8}$$

If $\frac{\pi}{2} - \phi \le 2\psi \le \frac{\pi}{2} - \phi + \tan^{-1}\left(\frac{0.5\sigma_f^r}{p\tan\phi + c}\right)$, it represents the intermediate mobilization of the reinforcement phase $-1 < \xi < 0$. In this case

$$R(\psi, p) = \frac{p\sin\phi + c\cos\phi}{\sin(2\psi + \phi)} \tag{9}$$

Finally, if $\frac{\pi}{2} - \phi + \tan^{-1}\left(\frac{0.5\sigma_f^r}{p\tan\phi + c}\right) \le 2\psi \le \pi$, it means that the yielding of the composite occurs with fully stressed reinforcement (in tension) $\xi = -1$

$$R(\psi, p) = -0.5\sigma_f^r\cos(2\psi) + \sqrt{\left[\left(p + 0.5\sigma_f^r\right)\sin\phi + c\cos\phi\right]^2 - 0.25\sigma_f^{r2}\sin^2(2\psi)} \tag{10}$$

## 2.2 Slip Line Method (SLM)

To apply the Slip Line Method (SLM) in the analysis of the bearing capacity of a footing on a reinforced soil slope, certain preliminary assumptions must be established: (a) The matrix phase, akin to soil, is treated as rigid-perfectly plastic; (b) The strip footing is considered rigid and weightless; (c) The matrix phase failure criterion adopts the associated flow rule; (d) The interface between the footing and the underlying medium is assumed to be fully smooth. Global equilibrium equations are formulated for stress characteristics as follows

$$\begin{cases} \frac{\partial \Sigma_x}{\partial x} + \frac{\partial \Sigma_{xz}}{\partial z} = 0 \\ \frac{\partial \Sigma_z}{\partial z} + \frac{\partial \Sigma_{xz}}{\partial x} = W \end{cases} \tag{11}$$

Stress components in the matrix phase can be reformulated in relation to R(ψ,p)

$$\begin{cases} \Sigma_x = p - R(\psi, p)\cos(2\psi) \\ \Sigma_z = p + R(\psi, p)\cos(2\psi) \\ \Sigma_{xz} = R(\psi, p)\sin(2\psi) \end{cases} \tag{12}$$

By substituting Eq.12 into the equilibrium equations (Eq. (11)), a set of hyperbolic equations is derived, solvable through the method of characteristics. The specifics of the arithmetic manipulations to create two groups of characteristic lines (α and β) can be referenced in (Jahanandish and Keshavarz 2005). Consequently, the stress characteristics along the characteristic $\alpha$-line can be articulated as

$$\frac{dz}{dx} = \tan(\psi - m - \mu) \tag{13a}$$

$$\frac{\sin 2(m-\mu)}{\cos(2m)}dp + \frac{2R(\psi, p)}{\cos(2m)}d\psi = -(\sin 2\mu dx + \cos 2\mu dz)F_x + (\cos 2\mu dx - \sin 2\mu dz)F_z \tag{13b}$$

and along the characteristic $\beta$-line

$$\frac{dz}{dx} = \tan(\psi - m + \mu) \tag{14a}$$

$$\frac{\sin 2(m+\mu)}{\cos(2m)}dp + \frac{2R(\psi, p)}{\cos(2m)}d\psi = (\sin 2\mu dx - \cos 2\mu dz)F_x + (\cos 2\mu dx + \sin 2\mu dz)F_z \tag{14b}$$

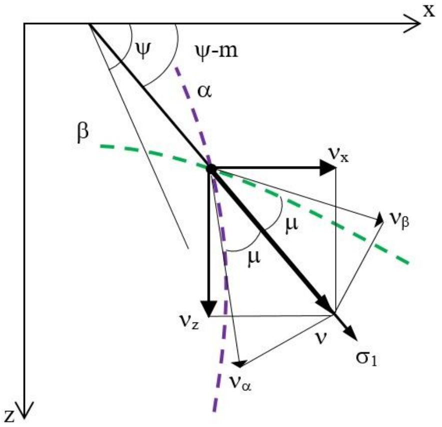

Fig. 4 Decomposition of velocity vector along *α* and *β* lines

where m and μ can be defined as follows (Michalowski and Zhao 1995)

$$m=\frac{1}{2}\tan\left[\frac{\partial R\left(\psi,p\right)}{2R\left(\psi,p\right)\partial\psi}\right]^{-1} \tag{15a}$$

$$\mu=\frac{1}{2}\cos\left[\cos(2m)\frac{\partial R\left(\psi,p\right)}{\partial p}\right]^{-1} \tag{15b}$$

Due to the assumption of the associated flow rule in the matrix phase, the stress characteristic lines align with the velocity characteristic lines, sharing identical equation formats. As depicted in Fig. 4, the velocity vector components, $v_x$ and $v_z$ along the x-axis and z-axis directions, are replaced by the tangential velocities of two groups of slip lines $v_\alpha$ and $v_\beta$

$$v_\alpha=v_x\cos(\psi-\mu)+v_z\sin(\psi-\mu) \tag{16a}$$

$$v_\beta=v_x\cos(\psi+\mu)+v_z\sin(\psi+\mu) \tag{16b}$$

By incorporating the definition of the associated flow rule and geometry equations, a unified expression for the velocity characteristic equations along the characteristic *α*-line can be derived, as detailed in Li *et al*. (2022)

$$\frac{dz}{dx}=\tan\left(\psi-m-\mu\right) \tag{17a}$$

$$\frac{dv_\alpha}{d\psi}=-v_\alpha\tan\phi+v_\beta\sec\phi \tag{17b}$$

and along characteristic *β*-line

$$\frac{dz}{dx}=\tan\left(\psi-m+\mu\right) \tag{18a}$$

$$\frac{dv_\beta}{d\psi}=v_\beta\tan\phi-v_\alpha\sec\phi \tag{18b}$$

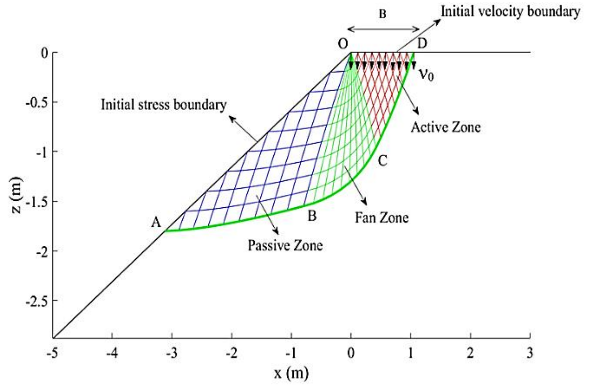

(a) $S_b$=0

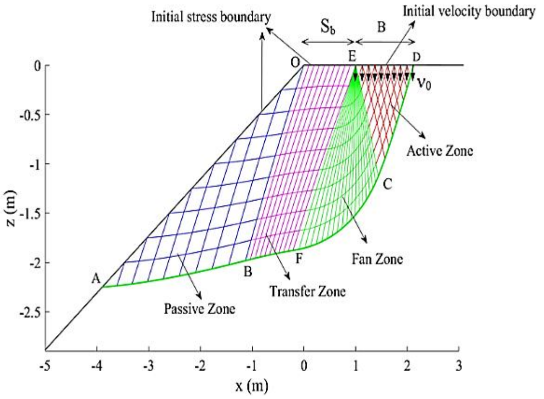

(b) $S_b \neq 0$

Fig. 5 Two failure modes based on the footing location on slope

### *2.3 Failure mode and critical slip surface*

This study focuses on the face failure, wherein the critical slip surface originates from the crest of the reinforced slope beneath the footing corner and terminates at a point on the slope surface, delineating the slope into a plastic region and a rigid region. It is important to note that the face failure scenario encompasses situations where the critical slip surface passes through the slope at the toe, with the elevation of the slip surface equal to the distance between the edge of the reinforced slope crest and the toe of the slope. Depending on the setback distance ($S_b$) between the footing and the edge of the slope crest, the face failure can be classified into two modes, as depicted in Fig. 5. In the absence of a setback distance, Fig. 5(a), the slip line field in the plastic region includes three distinct zones: Passive, Fan, and Active zones. With a setback distance, Fig. 5(b), it is assumed that four zones are generated, introducing the Transfer zone between the Passive and Fan zones. The slope surface (OA), representing a free boundary with no surcharge considered, serves as the initial stress boundary. The average stress (p) on this initial stress boundary is zero, and the direction angle $\psi$ is perpendicular to the boundary. The initial velocity boundary is defined by the footing load (OD or ED), where the velocity at the footing base $v_0$ is assumed to be 1 m/s, and the velocity direction aligns with the loading direction, i.e., vertical.

### *2.4 Boundary value problems*

Creating the slip line field requires solving boundary value problems, and in the domain of partial differential equations, three essential types of such problems (Cauchy, Riemann, and Mixed) are employed (Yu 2007), each tailored to a specific zone within the slip line. The Passive zone utilizes the Cauchy problem, whereas both the Fan and Transfer zones involve the Riemann problem. In the Active zone, the Mixed problem is applied. Fig. 6 provides a schematic diagram illustrating these three commonly used boundary value problems. Following the coordinate system, the initial boundary (OA) is discretized into minimal elements to determine coordinates (x and z) for grid points. In this study, a element length of 0.1B (where B = 1.0 m) is implemented at the initial boundary to ensure analytical precision. Once the values of the initial stress boundary (x,z,ψ, and p) are established, the finite difference method, coupled with a three-point technique, is commonly applied.

To illustrate the process of determining values (x,z,ψ, and p) for Point 21 (for instance), known values from Point 11 (or O) and Point 22, located on the initial stress boundary, are utilized. Fig. 6(a) provides a visual representation of this process. By substituting the known values of Point 22 and Point 11 into Eqs. (13) and (14), respectively, accounting for their positions relative to the α and β characteristic lines, the calculation proceeds along characteristic *α*-line as follows

$$\frac{z_{21}-z_{22}}{x_{21}-x_{22}}=\tan\left(\frac{\psi_{21}+\psi_{22}}{2}-m-\mu\right) \tag{19a}$$

$$\begin{aligned}&\frac{\sin 2(m-\mu)}{\cos(2m)}(p_{21}-p_{22})+\frac{R_{21}(\psi,p)+R_{22}(\psi,p)}{\cos(2m)}(\psi_{21}-\psi_{22})=\\&-\left[\sin 2\mu(x_{21}-x_{22})+\cos 2\mu(z_{21}-z_{22})\right]F_x+\left[\cos 2\mu(x_{21}-x_{22})-\sin 2\mu(z_{21}-z_{22})\right]F_z\end{aligned} \tag{19b}$$

and along characteristic *β*-line

$$\frac{z_{21}-z_{22}}{x_{21}-x_{22}}=\tan\left(\frac{\psi_{21}+\psi_{22}}{2}-m-\mu\right) \tag{19a}$$

$$\begin{aligned}&\frac{\sin 2(m-\mu)}{\cos(2m)}(p_{21}-p_{22})+\frac{R_{21}(\psi,p)+R_{22}(\psi,p)}{\cos(2m)}(\psi_{21}-\psi_{22})=\\&-\left[\sin 2\mu(x_{21}-x_{22})+\cos 2\mu(z_{21}-z_{22})\right]F_x+\left[\cos 2\mu(x_{21}-x_{22})-\sin 2\mu(z_{21}-z_{22})\right]F_z\end{aligned} \tag{19b}$$

and along characteristic *β*-line

$$\frac{z_{21}-z_{11}}{x_{21}-x_{11}}=\tan\left(\frac{\psi_{21}+\psi_{11}}{2}-m+\mu\right) \tag{20a}$$

$$\begin{aligned}&\frac{\sin 2(m-\mu)}{\cos(2m)}(p_{21}-p_{11})+\frac{R_{21}(\psi,p)+R_{11}(\psi,p)}{\cos(2m)}(\psi_{21}-\psi_{11})=\\&\left[\sin 2\mu(x_{21}-x_{11})-\cos 2\mu(z_{21}-z_{11})\right]F_x+\left[\cos 2\mu(x_{21}-x_{11})+\sin 2\mu(z_{21}-z_{11})\right]F_z\end{aligned} \tag{20b}$$

The iterative process is replicated to compute all grid points within the Passive zone. As an illustration, the determination of Point 32 involves computations based on Point 33 and Point 22, continuing in this manner. Subsequently, the points shared with the next zone (Transfer or Fan zone) are identified (OB). To generate the mesh in the Transfer zone, the initial stress boundary (OE) is established and divided, as mentioned earlier, with reference to the boundary (OA). Additionally, the boundary (OB) is determined from the preceding zone, as illustrated in Fig. 6(b). The values for Point 22 can be computed through Point 21 and Point 12 from the adjacent zone and

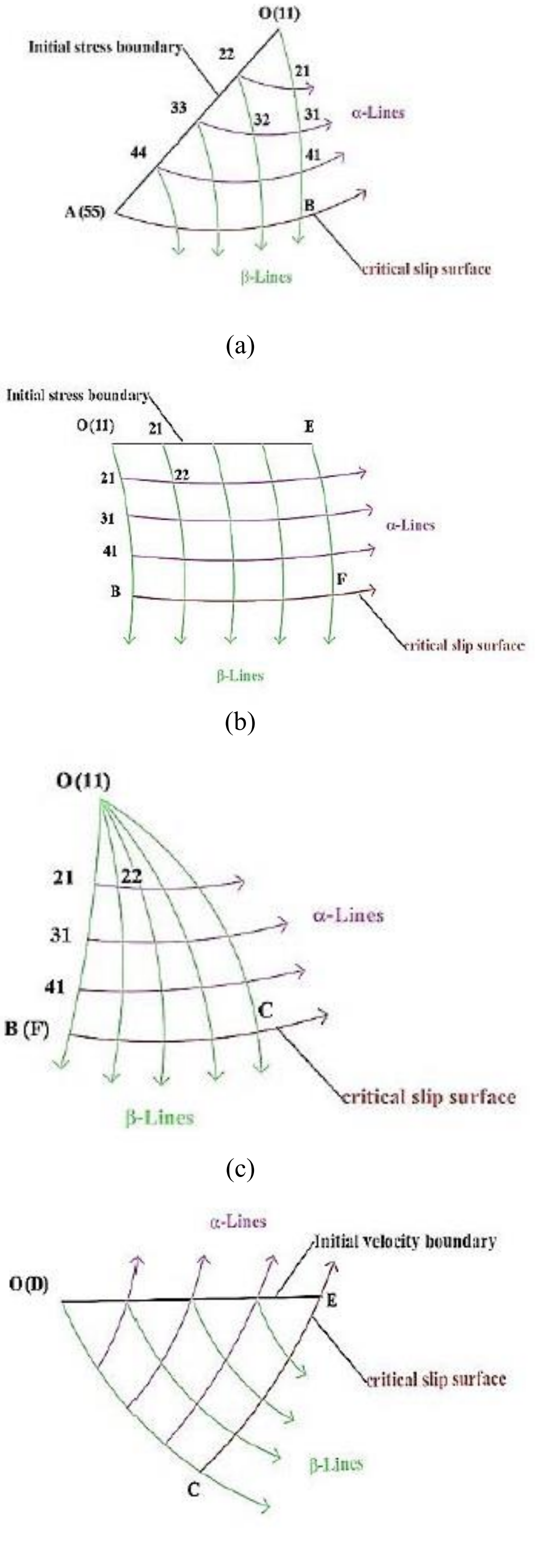

(a)

(b)

(c)

(d)

Fig. 6 Boundary value problems: (a) Passive zone, (b) Transfer zone, (c) Fan zone and (d) Active zone the initial stress boundary, respectively, using the previously outlined procedure. By iteratively applying this process, the points on the boundary (EF) and all points in the Transfer zone become known. As previously described, both Fan and Transfer zones constitute a Riemann problem, with the distinction that the initial stress boundary (OE) in the Transfer zone contracts to form a point referred to as the singular point (O) in the Fan zone, as depicted in Fig. 6(c). Employing the finite differences method and the three-point technique, the values for Point 22 are determined using the values of Point 11 and Point 21. This iterative process is replicated to compute the values for all points in the Fan zone, including the boundary points (OC), which are shared with the Active zone. For obtaining the grid points in the Active zone, the values of the boundary points (OC) and the mixed boundary points (OD or ED) are initially used by substituting them into the characteristic α-line (Eq. (13)). Subsequently, through the finite difference method and the three-point technique, the values for the remaining grid points in the active zone can be derived, as depicted in Fig. 6(d). With all grid point values determined, the stress slip line field is established.

### *2.5 Correlation between stress and velocity fields*

It is important to highlight that in stress slip lines, the originating boundary is (OA), while in velocity slip lines, the starting boundary is the initial velocity boundary (OD or ED). Given the consideration of the associated flow rule in this solution, the stress and velocity slip lines align in geometric space. Consequently, the coordinates ($x$, $z$, and $\psi$) of the grid points in the velocity field correspond to those in the stress field. Subsequently, the average stress p is replaced with the velocity vector $v$ in the finite difference equations (Eqs. (17) and (18)), facilitating the establishment of the velocity slip line field using the same three-point technique (Li and Jiang 2022). Once the slip line field is constructed, it is imperative to validate if the velocity along the critical slip surface conforms to the velocity discontinuity feature: $\Delta V_n = -\Delta V_t \tan\phi$, where $V_n$ and $V_t$ denote the normal and tangential velocity vectors along the critical slip surface, respectively. Meeting these conditions confirms that the solution for the bearing capacity of a footing placed on a reinforced slope is the exact solution, discernible as follows

$$q_u = \frac{1}{B}\sum_{1}^{n} p_i b_i \qquad b_i = x_{i+1} - x_i \tag{22}$$

where $x_1 = x_E$ and $x_n = x_D$. Alternatively, if the conditions are not met, the initial Point A needs to be re-selected, leading to a reconstruction of the slip line field using the aforementioned steps. Regarding the computing efficiency, the calculation for every step was completed within approximately 30 seconds. The computations were performed on an Intel(R) Core(TM) i7-2670QM CPU with 2.20GHz together with 16.0 GB RAM.

## 3. Comparison with other studies

In the context of static conditions, a comparative analysis can be extended to experimental investigations. In Fig. 7, the displacement vectors are presented for an laboratory test from centrifuge model experiments conducted by Sommers and Viswanadham (2009). These experiments aimed to explore the behavior of geotextile-reinforced slopes under the influence of loading applied to a strip footing near the slope crest. Fig. 7 illustrates the failure mechanism for the same scenario in the study by Ausilio (2014) and in the current study, represented by continuous lines. Upon scrutinizing the failure surfaces, it is evident that the depth of the failure surface derived from this study surpasses that computed through the upper bound approach employed by Ausilio (2014). Notably, the failure surface obtained from the Slip Line Method (SLM) exhibits a closer resemblance to the experimental findings, diverging from the characteristics of the upper bound solution. The surface obtained from SLM resembles much more to the experimental one rather than that of the upper bound solution. Regarding the comparison of the footing pressure at the point of failure from these two approaches, the centrifuge test produced an experimental value of 154 kPa, while the result from this study was 145 kPa, and the calculation in Ausilio's study resulted in 140 kPa.

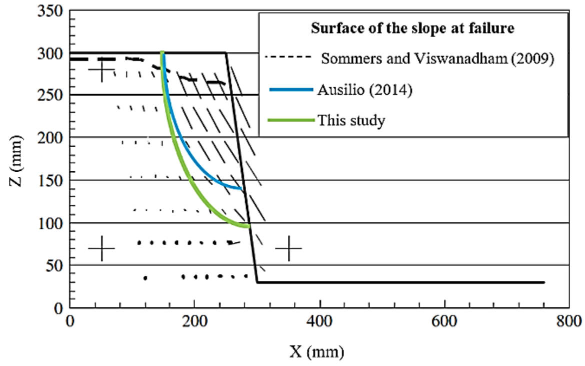

Fig. 7 Contrasting failure mechanism in proposed method and existing works

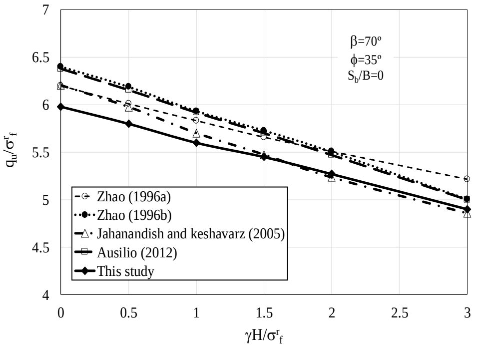

Fig. 8 Comparing the normalized ultimate bearing capacity between the present research and previous studies

The comparison for static state is illustrated in Fig. 8, where the normalized ultimate load $\frac{q_u}{\sigma_f^r}$ on reinforced slopes is depicted as functions of the dimensionless factor

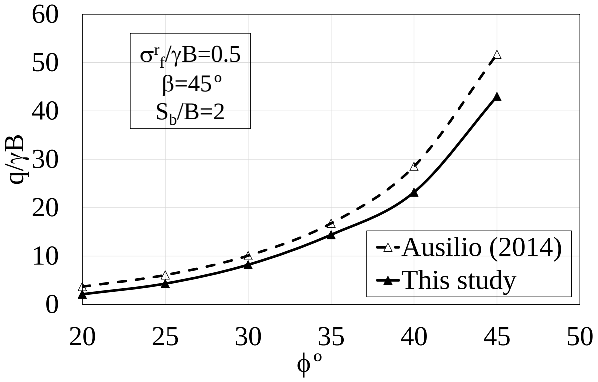

Fig. 9 Comparison of the normalized ultimate bearing capacity for footing placed on reinforced slope

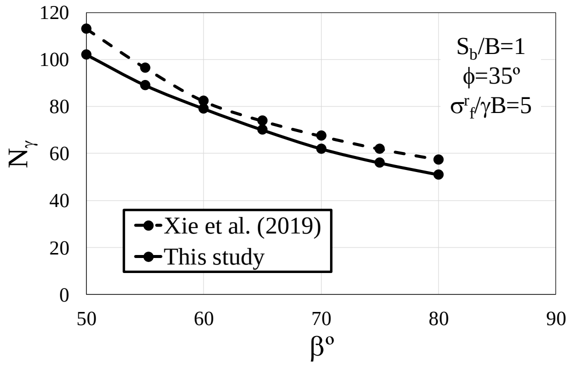

Fig. 10 Comparison of $N_\gamma$ values for footing placed on reinforced slope with setback ($S_b/B=1$)

$\frac{H_\gamma}{\sigma_f^r}$. The exact solution obtained from SLM in this study, incorporating a failure slip surface passing through the toe of the slope, is contrasted with the results derived from method of stress characteristics (Zhao 1996, Jahanandish and Keshavarz 2005) and upper bound limit analysis (Zhao 1996, Ausilio 2014).

The comparison of the normalized bearing capacity $\frac{q_u}{\gamma B}$ for a footing situated on a reinforced soil slope is illustrated in Fig. 9, considering various friction angles. The analysis results from this study are compared with outcomes derived using the kinematic theorem of upper-bound limit analysis, as exemplified by Ausilio (2014). For a slope angle $\beta = 45$, $S_b/B = 2$, and normalized tensile strength per unit cross-section, $\frac{\sigma_f^r}{\gamma B} = 2$, it is evident that the $\frac{q_u}{\gamma B}$ values obtained from the present analysis are comparatively lower than those determined by the kinematic theorem of upper-bound limit analysis.

In furtherance of the comparative investigation with previous research, an evaluative analysis was conducted to scrutinize the outcomes of the precise solution for the bearing capacity factor $N_\gamma$ associated with a footing positioned on a reinforced slope. It is reminded that the bearing capacity factor $N_\gamma$ is expressed as the ultimate bearing capacity ($q_u$) normalized with respect to the unit weight of the backfill ($\gamma$) and the width of the footing ($N_\gamma = q_u/(0.5\gamma B)$). The results are presented for diverse slope angles within the range of 50 to 80 degrees. Of particular relevance was the juxtaposition with the study conducted by Xie *et al.* (2019), wherein the limit equilibrium method served as the analytical framework. The meticulous examination was executed for a footing strategically situated at a distance of from the reinforced slope crest edge $S_b/B = 1$, normalized tensile strength $\frac{\sigma_f^r}{\gamma B} = 5$ and $\phi = 35$ degrees. The graphical representation in Fig.10 delineates a discernible convergence in the outcomes, notably conspicuous in scenarios where the slope inclination approximates 60 degrees.

## 4. Results and discussion

The principal aim of this research is to explore the impact of various factors, including backfill properties, structural geometry, and reinforcement strength, on the bearing capacity of strip footings situated on reinforced soil structures under static state. The ultimate goal is to provide valuable insights for preliminary design considerations. To facilitate a comprehensive interpretation of the findings, it is deemed appropriate to present the results in a non-dimensional format, considering the multitude of factors influencing bearing capacity. The calculations assume a cohesionless soil with a unit weight $\gamma$ of 20 kN/m³ and varying shearing resistance angles $\phi$ from 20° to 45°. Simultaneously, the slope incline angle $\beta$ is varied within the range of 10° to 70°. Design charts have been formulated to visually depict the outcomes of the bearing capacity factor $N_\gamma$ for a footing on a reinforced soil slope, accounting for different parameter values such as $\phi$ and $\beta$, with $S_b/B$ and $\sigma_f^r$ as additional variables. To gauge the efficacy of reinforcement in augmenting the bearing capacity of fill slopes, a meaningful comparison between the outcomes of the reinforced system and those of an unreinforced slope is essential. The benefits of incorporating reinforcements are quantified through the application of a non-dimensional parameter referred to as the Bearing Capacity Ratio (BCR). This ratio is defined as the ultimate bearing capacity of a footing on the reinforced slope $q_{ur}$ divided by the ultimate bearing capacity of a footing on the corresponding unreinforced slope $q_u$. The utilization of the BCR enables a quantitative assessment of the enhancement in bearing capacity attributed to the inclusion of reinforcement.

### *4.1 Effect of backfill shear strength*

The variation of bearing capacity factor $N_\gamma$ with soil internal friction angle $\phi$ and setback ratio $S_b/B$ is shown in Fig. 11. This variation is obtained for the slope incline angle $\beta$=30° and two magnitudes of $\sigma_f^r / \gamma B = 2,5$. The bearing capacity factor $N_\gamma$ exhibits exponential growth with the strength of the backfill. Notably, with the incorporation of closely spaced inclusion layers, strong reinforcements

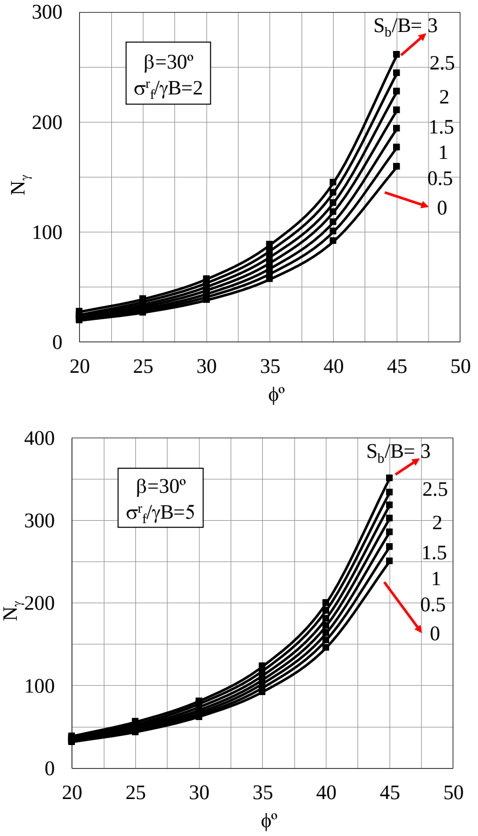

Fig. 11 Variation of $N_\gamma$ with friction angle $\phi$ at different setback values for two states: (a) $\sigma^r_f/\gamma B=2$ and (b) $\sigma^r_f/\gamma B=5$

$\sigma_f^r / \gamma B = 5$, the bearing capacity has the potential to increase by approximately 50% when a more realistic $\phi$ value of 45° is taken into account and $S_b/B=1$. Nevertheless, these advantages become less conspicuous in the presence of weaker overall reinforcement.

### *4.2 Effect of slope inclination angle*

The slope angle significantly impacts the bearing capacity of a footing on a reinforced soil slope. As depicted in Fig. 12, the bearing capacity factor $N_\gamma$ experiences a rapid decrease with the elevation of the slope angle $\beta$. This effect of $\beta$ remains consistent across various values of the setback distance $S_b$, soil internal friction angle $\phi=30°$, and tensile strength ratio $\sigma_f^r / \gamma B = 2,5$.

### *4.3 Effect of the tensile strength of inclusion layers*

The impact of the tensile strength of the inclusion layers on the ultimate bearing capacity factor $N_\gamma$ can be observed in Fig. 13. The graph depicts the bearing capacity factor $N_\gamma$ plotted against the tensile strength ratio $\sigma_f^r / \gamma B$ for various values of $S_b/B$, with $\phi = 30°$ with two magnitudes of $\beta = 30°$ and 70°. The results demonstrate that the bearing capacity factor $N_\gamma$ exhibits an upward trend as the tensile strength ratio and setback distance increase. However, the influence of the setback distance becomes nearly negligible for a slope with a large incline angle $\beta = 70°$.

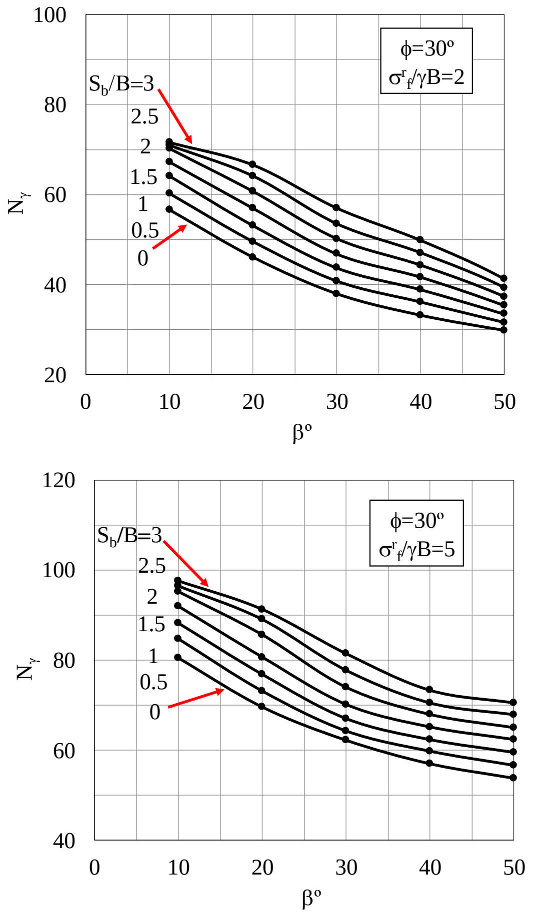

Fig. 12 Variation of $N_\gamma$ with slope angle β at different setback values for two states: (a) $\sigma^r_f/\gamma B=2$ and (b) $\sigma^r_f/\gamma B=5$

### *4.4 Effect of the setback distance*

The relationship between the Bearing Capacity Ratio (BCR) and the footing setback distance $S_b/B$ for different values of the tensile strength ratio is depicted in Fig.14. The analysis is carried out on a reinforced slope with a soil friction angle of $\phi = 40°$, considering two magnitudes of slope inclination $\beta = 30°$ and 60°. The results clearly show that the BCR exhibits an upward trend with an increase in the tensile strength ratio. The graphs illustrate that the influence of the footing setback distance $S_b/B$ on the BCR is more pronounced when strong inclusion elements (i.e. $\sigma_f^r / \gamma B = 5$) are utilized. However, when the inclusion elements are not sufficiently robust, the impact of the footing setback distance is not significant. It is noteworthy that as the setback distance increases, BCR decreases.

### *4.5 Distribution of reinforcement forces*

The recent findings of this study showcase the distribution of reinforcement forces beneath the footing

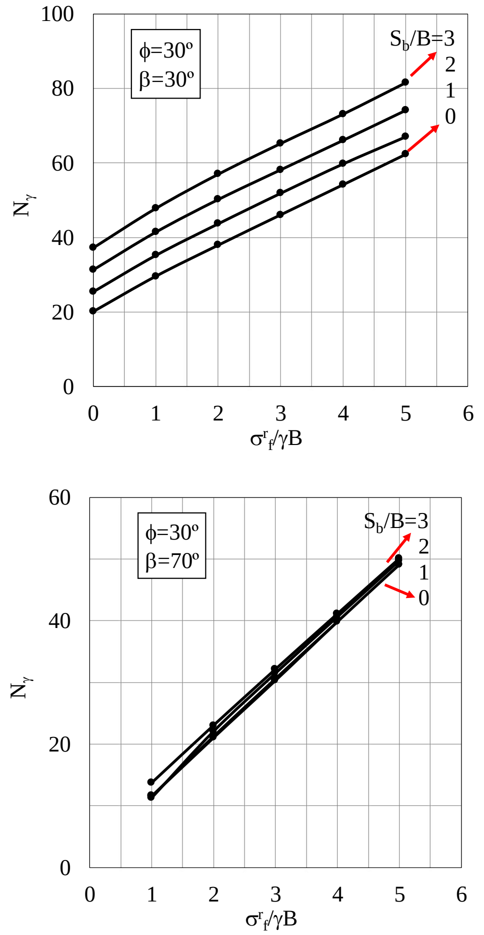

Fig. 13 Variation of $N_\gamma$ with $\sigma^r_f/\gamma B$ at different $S_b$ for two slope angle values: (a) β =30 degrees and (b) β =70 degrees

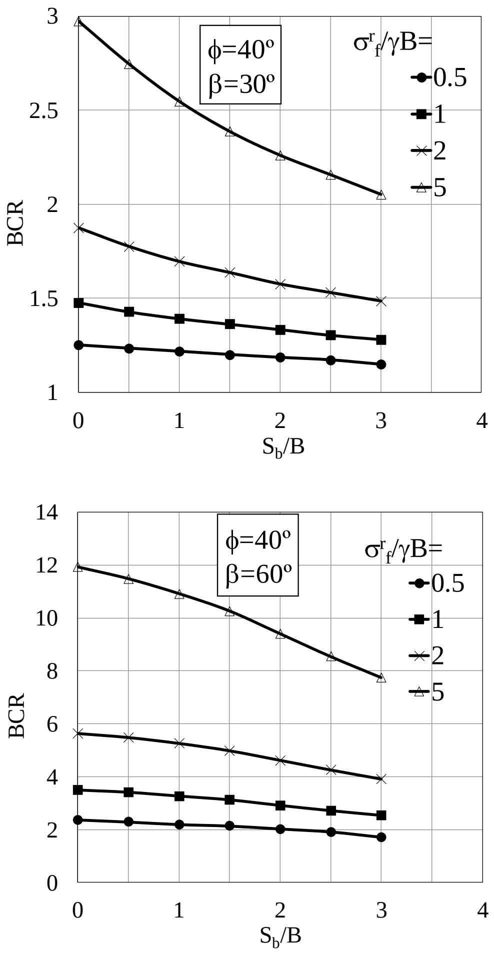

Fig. 14 Variation of BCR with $S_b/B$ at different $\sigma^r_f/\gamma B$ for two slope angle values: (a) β =30 degrees and (b) β =60 degrees

situated on the slope, illustrated through contour plots and colored curves in Fig. 15. Two distinct scenarios are considered based on the footing location. As previously mentioned, the mobilization coefficient of the reinforcement strength (ξ) ranges from 0 to -1, where a value of 0 indicates no influence from the inclusion elements, and a value of -1 signifies full engagement in tension. For values between 0 and -1, the inclusion elements act in an intermediate manner. In Fig. 15(a), where the footing is positioned at the edge of the slope, and Fig. 15(b), where it is located at a distance equal to the width of the footing, both scenarios assume a slope angle of 30 degrees, internal friction angle of the soil at 30 degrees, and tensile strength ratio $\sigma_f^r / \gamma B = 2$, under static state. Fig. 15(a) reveals that the distribution of reinforcement forces is concentrated directly beneath the footing (in the Active zone). In contrast, the force distribution decreases in the Fan zone and dissipates entirely in the Passive zone, indicating minimal influence of the reinforcement forces. This observation is reiterated in Fig. 15(b), where the impact of the inclusion elements is concentrated in the Active and Fan zones. Simultaneously, it begins to decrease in the Transfer zone and diminishes in the Passive zone.

Having determined the distribution of the mobilization coefficient (ξ) in the failure zone, one can derive the mobilized tensile stress in the reinforcement phase corresponding to each point in the failure zone. By assuming the desired layout of the inclusion layers including the thickness (t) and the spacing (d) throughout the reinforced soil slope, it is possible to find the tensile stress distribution along each inclusion layer by suing Eq. 3, i.e., $\sigma_x^{inc} = \sigma_x^r / \chi$ . For the two scenarios depicted in Fig. 15, it is assumed that the reinforced soil slopes are equipped with four inclusion layers with d = 0.4 m and t = 2 mm, which results in χ = 0.005. Fig. 16 depicts the tensile stress distribution along the layers inside the failure zone. In engineering practice, the tensile load along each inclusion layer can be calculated by the multiplication of $\sigma_x^{inc}$ by the layer thickness. It is figured out that the implication of SLM together with the two-phase approach, offer substantial utility for the design of the inclusion layers and their arrangement in the soil medium. For example, the designer can establish the optimal spacing between inclusion layers along with a specific thickness to attain the desired pattern

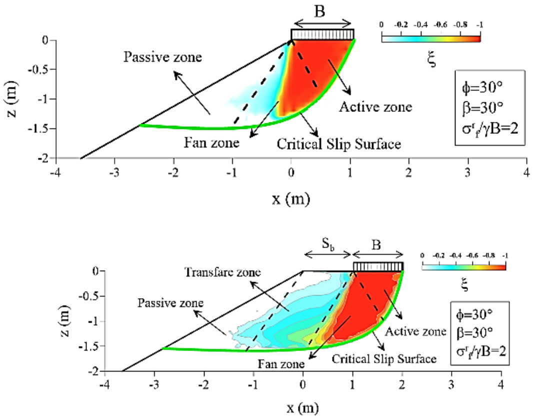

Fig. 15 The distribution of the mobilization coefficient of the reinforcement strength: (a) $S_b/B=0$ and (b) $S_b/B=1$

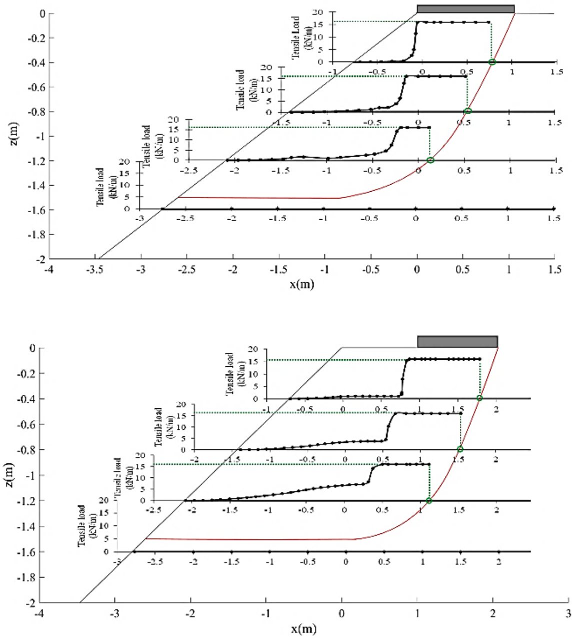

Fig. 16 The stress distribution along four inclusion layers by assuming a thickness of 2 mm and spacing of 0.4 m: (a) $S_b/B=0$ and (b) $S_b/B=1$

## 5. Conclusions

In this study, the exact bearing capacity of shallow strip footings in proximity to reinforced soil slopes has been meticulously examined through the integration of the two-phase approach, incorporating the slip line method. However, the two-phase approach has limitations. Specifically, it does not account for the pullout of reinforcement layers, and it precludes an examination of how the exact bearing capacity of strip footings is affected by the length of the reinforcement. Additionally, it is important to highlight that the two-phase approach is specifically applicable to reinforced soils with several inclusion layers such that a periodic medium exists representing a homogenous but anisotropic medium; its application for soils reinforced with a single inclusion layer is not supported or where the irregular layout of inclusion layers which might happen in non-ideal conditions. In this study, it is assumed that there is no slippage between the soil land inclusion layers which is only acceptable in case of dense and well-compacted soil. The utilization of this approach has led to significant advancements in accurately determining the critical slip surface by generating a comprehensive slip line field. The outcomes shed light on the impact of crucial parameters, including setback distance, slope angle, soil friction angle, and reinforcement strength, on the bearing capacity of the footings. These findings offer valuable insights for engineers and researchers engaged in the design of such structures. The principal objective of the research is to investigate the influence of diverse design parameters on the bearing capacity of these footings, with the key outcomes summarized as follows:

- The bearing capacity factor $N_\gamma$ exhibits an exponential growth with the strength of the backfill. Incorporating closely spaced and strong reinforcement layers can lead to a significant increase, up to 50%, when considering a more realistic internal friction angle $\phi = 45°$ and $S_b/B=1$. However, the benefits diminish with weaker overall reinforcement. Increasing the setback distance ($S_b$) from the slope face results in substantial improvements in bearing capacity for all given soil shear strengths.
- The slope angle $\beta$ significantly influences the bearing capacity, with $N_\gamma$ experiencing a rapid decrease as $\beta$ increases. This effect holds true across various values of setback distance ($S_b$), soil internal friction angle $\phi=$ 30, and tensile strength ratio $\sigma_f^r / \gamma B = 2 and\, 5$ .
- The ultimate bearing capacity factor $N_\gamma$ shows an upward trend with an increase in the tensile strength ratio and setback distance. However, the impact of the setback distance diminishes for steep slopes, rendering the effect negligible for an inclination angle of β = 70 degrees.
- The Bearing Capacity Ratio (BCR) displays an upward trend with an increase in the tensile strength ratio, with a more pronounced impact when strong inclusion elements are used. As the setback distance increases, BCR decreases, highlighting the diminishing returns on bearing capacity improvement.
- By knowing the reinforcement phase stress of each point in the failure zone, it is possible to calculate the tensile stress along the inclusion layers. These results can be significantly utilized for the design of the inclusion layer properties and their distribution in the soil medium.

The extensive outcomes of this study offer valuable insights into the behavior and design considerations of footings on reinforced soil slopes under static conditions. These findings can serve as a crucial point of reference for engineers and researchers engaged in the design of such systems. The incorporation of the slip line method, coupled with the exploration of diverse design parameters, enhances our comprehensive understanding of the bearing capacity and performance of footings on reinforced soil slopes.

Ultimately, this contributes to the development of safer and more effective engineering practices. In this investigation, the focus was exclusively on the analysis of cohesionless soil, without accounting for other soil types or the presence of cohesion. Future research endeavors should explore the influence of cohesion, especially in undrained clayey soils. While the study delved into the static state, a more in-depth examination of parameters such as inertia forces induced by earthquake loading is essential. Addressing these aspects in future research will advance the field, facilitating the development of more resilient static and seismic design strategies for footings on reinforced soil slopes.

## References

Acharyya, R. and Dey, A. (2018), "Assessment of bearing capacity and failure mechanism of single and interfering strip footings on sloping ground", *Int. J. Geotech. Eng.*, **15**(7), 822-833. https://doi.org/10.1080/19386362.2018.1540099.

Afsharpour, S., Payan, M., Chenari, R.J., Ahmadi, H. and Fathipour, H. (2022), "Bearing capacity of strip footings on unsaturated soils under combined loading using LEM", *Geomech. Eng.*, **31**(2): 223-235. https://doi.org/10.12989/gae.2022.31.2.223.

Afzali-Nejad, A., Lashkari, A. and Martinez, A. (2021), "Stress-displacement response of sand–geosynthetic interfaces under different volume change boundary conditions", *J. Geotech. Geoenviron. Eng.*, **147**(8), 04021062. https://doi.org/10.1061/(ASCE)GT.1943-5606.0002544.

Ahmadi, R., Jahromi, S.G. and Shabakhty, N. (2022), "Reliability analysis of external and internal stability of reinforced soil under static and seismic loads", *Geomech. Eng.*, **29**(6), 599-614. https://doi.org/10.12989/gae.2022.29.6.599.

Ardakani, A. and Namaei, A. (2021), "Numerical investigation of geocell reinforced slopes behavior by considering geocell geometry effect", *Geomech. Eng.*, **24**(6), 589-597. https://doi.org/10.12989/gae.2021.24.6.589.

Ausilio, E. (2014), "Seismic bearing capacity of strip footings located close to the crest of geosynthetic reinforced soil structures", *Geotech. Geol. Eng.*, **32**(4), 885-899. https://doi.org/10.1007/s10706-014-9765-4.

Chakraborty, D. and Kumar, J. (2013), "Bearing capacity of foundations on slopes", *Geomech. Geoeng.*, **8**(4), 274-285. https://doi.org/10.1080/17486025.2013.770172.

de Buhan, P. and Sudret, B. (1999), "A two-phase elastoplastic model for unidirectionally-reinforced materials", *Eur. J. Mech. - A/Solids*, **18**(6), 995-1012. https://doi.org/10.1016/S0997-7538(99)00109-6.

Gholami, H. and Seyedi Hosseininia, E. (2017), "Bearing capacity factors of ring footings by using the method of characteristics", *Geotech. Geol. Eng.*, **35**(5), 2137-2146. https://doi.org/10.1007/s10706-017-0233-9.

Halder, K. and Chakraborty, D. (2020), "Probabilistic bearing capacity of strip footing on reinforced anisotropic soil slope", *Geomech. Eng.*, **23**(1), 15-30. https://doi.org/10.12989/gae.2020.23.1.015.

Halder, K., Chakraborty, D. and Kumar Dash, S. (2019), "Bearing capacity of a strip footing situated on soil slope using a non-associated flow rule in lower bound limit analysis", *Int. J. Geotech. Eng.*, **13**(2), 103-111. https://doi.org/10.1080/19386362.2017.1325119.

Hassine, W.B., Hassis, H. and de Buhan, P. (2008), "A macroscopic model for materials reinforced by flexible membranes", *Mech. Res. Commun.*, **35**(5), 310-319. https://doi.org/10.1016/j.mechrescom.2008.02.009.

Honari, S. and Seyedi Hosseininia, E. (2016), "Numerical Modeling of Reinforced Soil Walls Using Multiphase Approach and Hyperbolic Constitutive Model".

Jahanandish, M. and Keshavarz, A. (2005), "Seismic bearing capacity of foundations on reinforced soil slopes", *Geotext. Geomembranes*, **23**(1), 1-25

Javdanian, H. (2017), "On the behaviour of shallow foundations constructed on reinforced soil slope – a numerical analysis", *Int. J. Geotech. Eng.*, **14**(2), 188-195. https://doi.org/10.1080/19386362.2017.1416971.

Li, C. and Jiang, P. (2022), "Method of rigorous characteristics for seismic bearing capacity of strip footings Placed adjacent to homogeneous soil slopes", *Int. J. Geomech.*, **22**(10), 04022179. https://doi.org/10.1061/(ASCE)GM.1943-5622.0002526.

Luo, N. and Bathurst, R.J. (2017), "Reliability bearing capacity analysis of footings on cohesive soil slopes using RFEM", *Comput. Geotech.*, **89**: 203-212. https://doi.org/10.1016/j.compgeo.2017.04.013.

Luo, N. and Bathurst, R.J. (2018), "Deterministic and random FEM analysis of full-scale unreinforced and reinforced embankments", *Geosynth. Int.*, **25**(2), 164-179. https://doi.org/10.1680/jgein.17.00040.

Manna, D., Santhoshkumar, G. and Ghosh, P. (2021), "Upper-bound limit load of rigid pavements resting on reinforced soil embankments – Kinematic approach", *Transport. Geotech.*, **30**, 100611. https://doi.org/10.1016/j.trgeo.2021.100611.

Michalowski, R.L. and Zhao, A. (1995), "Continuum versus structural approach to stability of reinforced soil", *J. Geotech. Eng.*, **121**(2), 152-162. https://doi.org/10.1061/(ASCE)0733-9410(1995)121:2(152).

Nasrollahi, S.M. and Seyedi Hosseininia, E. (2019), "A simplified solution for piled-raft foundation analysis by using the two-phase approach", *Comptes Rendus Mécanique*, **34**(10), 716-733. https://doi.org/10.1016/j.crme.2019.10.002

Sarfarazi, V., Tabaroei, A. and Asgari, K. (2022), "Discrete element modeling of strip footing on geogrid-reinforced soil", *Geomech. Eng.*, **29**(4), 435-449. https://doi.org/10.12989/gae.2022.29.4.435.

Sarvesh, R., Srinivasan, V. and Patel, A. (2023), "Finite element limit analysis of the bearing capacity of an obliquely loaded strip footing on granular soil placed adjacent to vertically loaded existing footing", *Geomech. Eng.*, **35**(3), 287-306. https://doi.org/10.12989/gae.2023.35.3.287.

Seyedi Hosseininia, E. and Ashjaee, A. (2018). "Numerical simulation of two-tier geosynthetic-reinforced-soil walls using two-phase approach", *Comput. Geotech.*, **100**, 15-29. https://doi.org/10.1016/j.compgeo.2018.04.003.

Seyedi Hosseininia, E. and Farzaneh, O. (2010), "Development and validation of a two-phase model for reinforced soil by considering nonlinear behavior of matrix", *J. Eng. Mech.* **136**(6), 721-735. https://doi.org/10.1061/(ASCE)EM.1943-7889.0000111.

Seyedi Hosseininia, E. and Farzaneh, O. (2010), "A simplified two-phase macroscopic model for reinforced soils", *Geotextiles and Geomembranes* **28**(1): 85-92.https://doi.org/10.1016/j.geotexmem.2009.09.009

Seyedi Hosseininia, E. and Farzaneh, O. (2011), "A non-linear two-phase model for reinforced soils", *Proceedings of the Institution of Civil Engineers - Ground Improvement*, **164**(4), 203-211. https://doi.org/10.1680/grim.9.00039.

Sommers, A.N. and Viswanadham, B.V.S. (2009), "Centrifuge model tests on the behavior of strip footing on geotextile-reinforced slopes", *Geotext. Geomembranes*, **27**(6), 497-505. https://doi.org/10.1016/j.geotexmem.2009.05.002.

Tarraf, M. and Seyedi hosseininia, E. (2023), "Pullout capacity of horizontal circular plates embedded in sand using the method of stress characteristics", *Mar. Georesour. Geotec.,* https://doi.org/10.1080/1064119X.2023.2287145

Wang, Z., Jacobs, F., Ziegler, M. and Yang, G. (2020), "Visualisation and quantification of geogrid reinforcing effects under strip footing loads using discrete element method", *Geotext. Geomembranes*, **48**(1), 62-70. https://doi.org/10.1016/j.geotexmem.2019.103505.

Xie, Y., Leshchinsky, B. and Han, J. (2019), "Evaluation of bearing capacity on geosynthetic-reinforced soil structures considering multiple failure mechanisms", *J. Geotech. Geoenviron. Eng*., **145**(9), 04019040. https://doi.org/10.1061/(ASCE)GT.1943-5606.0002072

Xu, P., Li, C., Hatami, K., Yang, G. and Liang Xunmei, X. (2022), "Finite element limit analysis of load-bearing performance of reinforced slopes using a non-associated flow rule", *Geotext. Geomembranes*, **50**(5), 1020-1035. https://doi.org/10.1016/j.geotexmem.2022.07.002.

Yu, H.S. (2007), Plasticity and geotechnics, Springer Science & Business Media.

Zhao, A. (1996), "Failure loads on geosynthetic reinforced soil structures", *Geotext. Geomembranes*, **14**(5), 289-300. https://doi.org/10.1016/0266-1144(96)89796-2.

Zhao, A. (1996), "Limit analysis of geosynthetic-reinforced soil slopes", *Geosynth. Int.*, **3**(6), 721-740. https://doi.org/10.1680/gein.3.0082.

*CC*